chemosensors

Article

Construction of 2D TiO_2@MoS_2 Heterojunction Nanosheets for Efficient Toluene Gas Detection

Dehui Wang, Jinwu Hu, Hui Xu *, Ding Wang and Guisheng Li

School of Materials and Chemistry, University of Shanghai for Science & Technology, Shanghai 200093, China; wangding@usst.edu.cn (D.W.); liguisheng@usst.edu.cn (G.L.)
* Correspondence: xuhui@usst.edu.cn

Abstract: Monitoring trace toluene exposure is critical for early-stage lung cancer screening via breath analysis, yet conventional chemiresistive sensors face fundamental limitations, including compromised selectivity in complex VOC matrices and humidity-induced signal drift, with prevailing p–n heterojunction architectures suffering from inherent charge recombination and environmental instability. Herein, we pioneer a 2D core–shell n–n heterojunction strategy through rational design of TiO_2@MoS_2 heterostructures, where vertically aligned MoS_2 nanosheets are epitaxially grown on 2D TiO_2 derived from graphene-templated synthesis, creating built-in electric fields at the heterojunction interface that dramatically enhance charge carrier separation efficiency. At 240 °C, the TiO_2@MoS_2 sensor exhibits a superior response (R_a/R_g = 9.8 to 10 ppm toluene), outperforming MoS_2 (R_a/R_g = 2.8). Additionally, the sensor demonstrates rapid response/recovery kinetics (9 s/16 s), a low detection limit (50 ppb), and excellent selectivity against interfering gases and moisture. The enhanced performance is attributed to unidirectional electron transfer ($TiO_2 \rightarrow MoS_2$) without hole recombination losses, methyl-specific adsorption through TiO_2 oxygen vacancy alignment, and steric exclusion of non-target VOCs via size-selective MoS_2 interlayers. This work establishes a transformative paradigm in gas sensor design by leveraging n–n heterojunction physics and 2D core–shell synergy, overcoming long-standing limitations of conventional architectures.

Keywords: heterojunction; TiO_2@MoS_2; nanosheet; synergistic effects; toluene gas sensor

check for updates

Received: 15 March 2025
Revised: 14 April 2025
Accepted: 18 April 2025
Published: 22 April 2025

Citation: Wang, D.; Hu, J.; Xu, H.; Wang, D.; Li, G. Construction of 2D TiO_2@MoS_2 Heterojunction Nanosheets for Efficient Toluene Gas Detection. *Chemosensors* **2025**, *13*, 154. https://doi.org/10.3390/chemosensors13050154

Copyright: © 2025 by the authors. Licensee MDPI, Basel, Switzerland. This article is an open access article distributed under the terms and conditions of the Creative Commons Attribution (CC BY) license (https://creativecommons.org/licenses/by/4.0/).

1. Introduction

Toluene is a common volatile organic compound (VOC) that can damage the central nervous system, causing headaches, dizziness, and liver and kidney toxicity with long-term exposure. High-concentration inhalation can lead to acute poisoning. Toluene also serves as a potential biomarker for diagnosing diseases like lung cancer and diabetes [1]. Traditional detection methods, such as gas chromatography–mass spectrometry (GC-MS), are accurate, but require expensive equipment and laboratory settings, preventing real-time monitoring. Electrochemical sensors face cross-interference issues, and photoionization detectors (PIDs) are costly to maintain. Therefore, developing high-sensitivity, low-cost, portable semiconductor toluene gas sensors through material innovation and intelligent design is crucial [2–4]. Such sensors could enable home health monitoring, industrial safety warnings, and early disease screening, promoting advancements in precision medicine and environmental governance [5].

Two-dimensional transition metal dichalcogenides (TMDs) have emerged as promising candidates for next-generation gas sensors, due to their atomic-scale thickness, tunable

electronic properties, and high surface-to-volume ratios [6]. Molybdenum disulfide (MoS_2), a graphene-like layered TMD, has garnered significant attention. In its thermodynamically stable 2H phase, the crystal structure consists of S-Mo-S trilayers stacked via van der Waals interactions, with each Mo atom in trigonal prismatic coordination [7–9]. The hydrothermal synthesis of MoS_2 enables precise control over layer number (typically one to five layers) and defect density, yielding nanostructures with specific surface areas and direct bandgaps suitable for charge transfer-based gas sensors [10,11]. Notably, 2D MoS_2 nanosheets exhibit superior gas adsorption kinetics compared to their 0D quantum dot or 1D nanobelt due to their exposed basal planes (90% surface accessibility) and abundant edge sulfur vacancies, which serve as preferential adsorption sites [12]. Additionally, in the case of ultrathin MoS_2 layers, the sulfide terminations at MoS_2 edges can achieve maximal exposure. Thus, constructing heterostructures to vertically grow such thin 2D MoS_2 represents a viable strategy [13].

Heterojunction engineering effectively enhances sensing performance by lowering operating temperatures and improving sensitivity, selectivity, and humidity resistance in nanomaterials [14,15]. Due to the band structure mismatch between two sensing materials, energy bands bend to form electron- depletion layers (EDLs) or hole accumulation layers (HALs) when the Fermi levels equilibrate [16,17]. Furthermore, a hierarchical composite structure can provide additional active adsorption sites for target gases and exhibit superior catalytic activity compared to single metal oxides. Thus, heterostructures are critical for optimizing the gas-sensing properties of metal oxides [18,19]. Hermawan et al. [20] reported a p–n CuO@SnO_2 heterojunction that achieved a remarkable toluene response (R_a/R_g = 540 at 75 ppm) with exceptional selectivity. The enhanced performance was attributed to the synergistic effects of the p–n heterojunction, high surface area, and porous architecture. Notably, in situ formation of metallic Cu under high toluene concentrations disrupted the p–n junction and established Ohmic contact with the n-type SnO_2, further amplifying the sensing response. Liu et al. [21] fabricated a porous Co_3O_4–Fe_3O_4 composite with p–n heterojunctions by functionalizing Fe_3O_4 with ZIF-67-derived Co_3O_4. The Co_3O_4 derived from ZIF-67 exhibited a higher specific surface area than Fe_3O_4, leading to a 20-fold improvement in toluene response at 225 °C. Additionally, the sensor demonstrated a low detection limit (0.1 ppm, response = 1.68), excellent selectivity, and long-term stability. This enhancement primarily stemmed from the p–n heterojunction, increased surface area, and optimized oxygen vacancy (O_V) concentration. Therefore, heterojunction construction provides a viable pathway for developing highly sensitive and practical gas sensors based on nanostructured metal oxides. The integration of vertically aligned ultrathin MoS_2 nanosheets with a wide-bandgap metal oxide semiconductor (MOS) core constructs a 2D core–shell n–n heterojunction, where the MOS core acts as an electron donor and the MoS_2 shell serves as an electron acceptor [14]. A built-in electric field forms at the heterointerface through type II band alignment, significantly enhancing carrier separation efficiency, while the core–shell structure achieves specific gas recognition through the synergistic interface coupling effect between MOS and MOS_2 components [6].

Here, we report a unique 2D heterostructure TiO_2@MoS_2 nanosheet. Two-dimensional TiO_2 nanosheets were synthesized via a graphene sacrificial template method, followed by the hydrothermal growth of fish scale-like MoS_2 nanosheets on their surfaces. By adjusting the hydrothermal reaction time, MoS_2 layers with controlled thicknesses were achieved, exhibiting an average lateral size of 193 ± 21 nm. Compared to pristine MoS_2 nanosheets, the TiO_2@MoS_2 heterostructure demonstrated a superior toluene response (R_a/R_g = 9.8@10 ppm) at 240 °C, along with rapid response/recovery kinetics (9 s/16 s), excellent stability, durability, and high humidity resistance. The enhanced gas-sensing performance is attributed to the n–n heterojunction and high specific surface area. The

synergistic interaction between the two components and the unique core–shell hierarchical architecture with self-assembled nanostructures collectively amplify the sensor's capabilities. This study provides a rational material design strategy, offering a promising candidate for efficient detection of toluene gas.

2. Materials and Methods

2.1. Synthesis of Sensor Materials

Synthesis of TiO_2 Nanosheets: TiO_2 precursor was synthesized using a graphene oxide (GO) sacrificial template method. Specifically, 100 mg of GO was dispersed in 200 mL of ethanol and ultrasonicated for 1 h. Subsequently, 2.5 mmol of titanium butoxide (TBOT) was added dropwise under continuous stirring, and the mixture was stirred overnight (18 h) to obtain a gray suspension. The product was thoroughly washed three times with deionized water and ethanol, followed by drying at 80 °C overnight. Finally, the dried powder was calcined in a muffle furnace at 500 °C for 2 h with a heating rate of 2 °C/min, yielding white TiO_2 nanosheets.

Synthesis of TiO_2@MoS_2 Nanocomposites: 0.1 mmol of ammonium heptamolybdate tetrahydrate $(NH_4)_2MoO_4{\cdot}4H_2O$) was dissolved in 10 mL of deionized water under vigorous stirring. A predetermined amount of the as-prepared TiO_2 nanosheets was added to the solution, and the mixture was incubated at room temperature for 12 h and dried at 80 °C for 12 h. Separately, 0.1 mmol of $(NH_4)_2MoO_4{\cdot}4H_2O$ and 3.05 mmol of thiourea (CH_4N_2S) were dissolved in 40 mL of deionized water. The $(NH_4)_2MoO_4{\cdot}4H_2O$-loaded TiO_2 nanosheets were then added to the solution, and the mixture was stirred at room temperature for 1 h. The homogeneous suspension was transferred to a 50 mL Teflon-lined stainless-steel autoclave and heated at 200 °C for 8 h. After cooling to room temperature, the black precipitate was collected, washed three times with deionized water and ethanol, and dried at 60 °C overnight to obtain TiO_2@MoS_2-8 nanosheets. By adjusting the reaction time to 4 h and 12 h under identical conditions, samples labeled TiO_2@MoS_2-4 and TiO_2@MoS_2-12 were prepared. For comparison, pure MoS_2 nanosheets were synthesized using the same procedure without the addition of TiO_2 nanosheets.

2.2. Gas-Sensing Performance Measurement

The as-prepared TiO_2 NSs, TiO_2@MoS_2 NSs, and MoS_2 NSs were mixed with deionized water to form a homogeneous paste. Each paste was uniformly coated onto a ceramic substrate equipped with a pair of gold electrodes using a fine brush (Figure S1). The operating temperature of the sensor was controlled by adjusting the heating current applied to the embedded heating electrode. The gas-sensing performance was evaluated using a static test system (Elite Technology Co., Ltd. Suzhou, China). Target gas concentrations were generated via a static gas distribution method.

The gas-sensing performance was evaluated using a custom-built static testing system, where sensor resistance was monitored continuously with a source meter under controlled conditions. Target analytes were introduced into the 20 L test chamber by injecting liquid toluene with a microsyringe and vaporizing it on a hotplate. The volume Q can be determined by:

$$Q = \frac{VCM}{22.4D\rho} \times 10^{-9} \times \frac{273 + T_R}{273 + T_B} \quad (1)$$

Here, V, C, M, d, ρ, T_R, and T_B are the test chamber volume (L), vapor concentration (ppm), molecular mass (g/mol), liquid density (kg/m^3), liquid purity (%), environmental temperature (°C), and temperature (°C) in the testing chamber, respectively.

Sensitivity (S), a critical performance metric of gas sensors, is quantified as the resistance ratio under distinct gaseous environments. For n-type semiconductors, sensitivity is defined as:

$$S = R_a / R_g \ (N - type) \ (oxidizing \ gases) \quad (2)$$

$$S = R_g / R_a \ (N - type) \ (reducing \ gases) \quad (3)$$

where R_a denotes the baseline resistance in dry air and R_g represents the steady-state resistance upon exposure to the target analyte. Conversely, p-type semiconductors exhibit inverse trends.

3. Results and Discussion

3.1. Morphology and Structure Characterization

As demonstrated in Figure 1, TiO_2 nanosheets were synthesized via a graphene oxide sacrificial template method followed by annealing at 500 °C. Subsequently, fish scale-like MoS_2 nanosheet arrays were uniformly grown on the TiO_2 surfaces through a controlled hydrothermal reaction (Figure 1). Optimizing precursor concentration and hydrothermal reaction time was crucial for MoS_2 growth. The thickness of MoS_2 nanostructures could be effectively tuned by adjusting the hydrothermal duration. The facile and reproducible synthesis protocol offers significant advantages for scalable production.

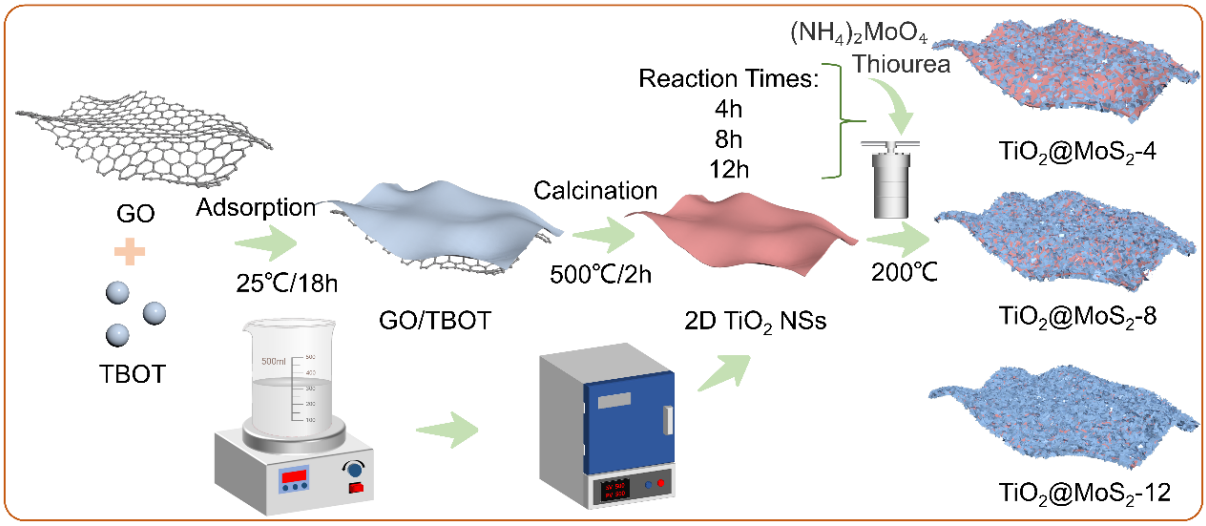


Figure 1. Schematic illustration of the synthesis process for TiO_2@MoS_2 nanosheets via a graphene oxide sacrificial template combined with hydrothermal reaction.

To characterize the morphology and structure of TiO_2@MoS_2 composites, SEM and low-magnification TEM analyses were performed. As shown in Figure 2a, ultrathin TiO_2 nanosheets (~2.1 ± 0.3 nm thickness) were successfully synthesized via the graphene oxide sacrificial template method. In contrast, pristine MoS_2 formed spherical aggregates with an average diameter of 530 ± 12 nm (Figure 2b). Figure 2c–e reveal the hierarchical heterostructure, where vertically aligned MoS_2 nanosheets (193 ± 21 nm lateral size) uniformly coat TiO_2 surfaces, forming an n–n heterojunction. The MoS_2 coverage density exhibited a positive correlation with hydrothermal duration, enabling thickness-controlled growth. TEM characterization (Figure 2f) further confirmed the 2D–2D interfacial architecture. HR-TEM analysis (Figure 2g) resolved distinct lattice spacings of 0.250 nm, corresponding to the (102) plane of MoS_2 [22–25]. The polycrystalline nature was verified by selective electron diffraction (SAED) patterns showing concentric diffraction rings (Figure 2h). Energy dispersion spectrum (EDS) elemental mapping (Figure 2i) demonstrated homogeneous spatial

distribution of Ti, Mo, S, and O, conclusively confirming the formation of well-integrated TiO_2@MoS_2 heterostructures.

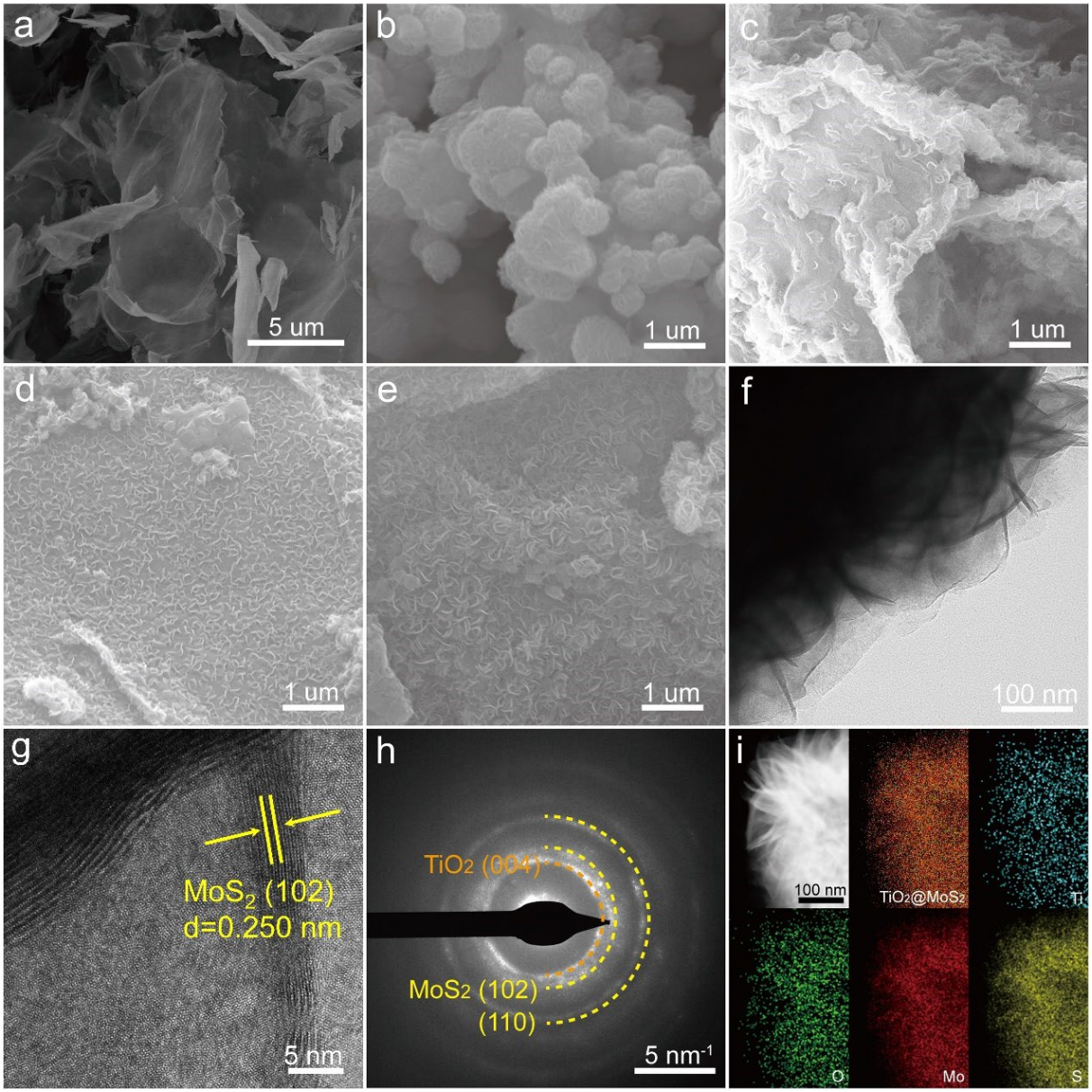


Figure 2. Morphological and structural characterization of TiO_2@MoS_2 heterostructures: SEM images of (**a**) TiO_2, (**b**) MoS_2, (**c**) TiO_2@MoS_2-4, (**d**) TiO_2@MoS_2-8, and (**e**) TiO_2@MoS_2-12; (**f**–**i**) TEM, HR-TEM, SAED, and EDS elemental mapping images of TiO_2@MoS_2-8, respectively.

To determine the phase composition and interfacial interactions in the TiO_2@MoS_2 heterostructure, X-ray diffraction (XRD) and Raman analyses were performed. The XRD pattern of TiO_2@MoS_2 (Figure 3a) revealed distinct diffraction peaks at 25.3° (101), 37.8° (004), and 48.0° (200), corresponding to anatase TiO_2 (JCPDS #97-002-4276), alongside peaks at 31.6° (102) and 45.5° (110), attributed to MoS_2 (JCPDS #97-064-4259). A noticeable shift in the (004) peak of TiO_2 and the (110) peak of MoS_2 was observed, indicative of lattice strain arising from the intimate interfacial coupling in the heterojunction.

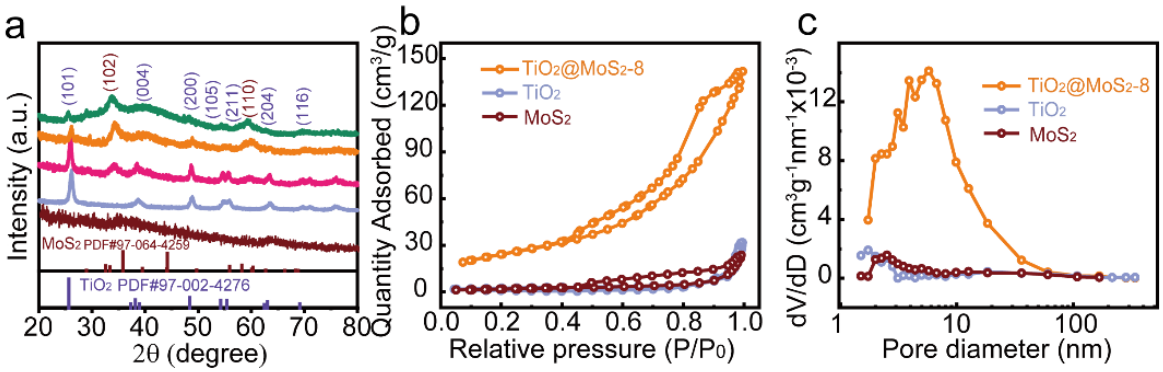


Figure 3. (**a**) XRD patterns of TiO_2, MoS_2, TiO_2@MoS_2-4 (pink line), TiO_2@MoS_2-8 (orange line), and TiO_2@MoS_2-12 (green line) samples; (**b**,**c**) nitrogen adsorption–desorption isotherms and BJH pore size distribution of TiO_2, MoS_2, and TiO_2@MoS_2-8.

To analyze the structural advantages of the TiO_2@MoS_2 nanocomposite, nitrogen adsorption–desorption measurements were conducted to determine its specific surface area and pore distribution using BET theory and BJH methods. As shown in Figure 3b, all three materials (TiO_2, MoS_2, TiO_2@MoS_2-8) exhibit type IV isotherms with H3-type hysteresis loops in the relative pressure (P/P_0) range of 0.6–1.0, characteristic of mesoporous structures. The average pore diameters determined by BJH analysis were 2.4 nm (TiO_2), 3.1 nm (MoS_2), and 8.3 nm (TiO_2@MoS_2-8). Notably, the TiO_2@MoS_2-8 composite demonstrated the highest BET surface area of 87.48 m^2/g, significantly surpassing that of pristine TiO_2 nanosheets (9.04 m^2/g) and MoS_2 nanosheets (19.68 m^2/g), confirming the heterojunction's role in enhancing porosity (Figure 3c).

X-ray photoelectron spectroscopy (XPS) was employed to investigate the surface composition and chemical states of TiO_2, MoS_2, and TiO_2@MoS_2-8 nanocomposites. As shown in Figure 4a, the survey spectra confirm the coexistence of Ti, Mo, S, and O in the TiO_2@MoS_2-8 heterostructure, consistent with EDS, XRD, and HRTEM results, with no impurity peaks except for residual carbon (C 1s). High-resolution Ti 2p spectra (Figure 4b) reveal characteristic peaks at 459.08 eV (Ti $2p_{3/2}$) and 464.87 eV (Ti $2p_{1/2}$) for TiO_2@MoS_2-8, with a spin–orbit splitting of 5.79 eV, typical of Ti^{4+} in TiO_2. Notably, a 0.40 eV positive binding energy shift compared to pure TiO_2 (458.68 eV and 464.47 eV) indicated electron transfer from TiO_2 to MoS_2. The Mo 3d spectrum (Figure 4c) exhibited peaks at 228.65 eV (Mo $3d_{5/2}$) and 231.87 eV (Mo $3d_{3/2}$), with a corresponding S 2s peak at 225.90 eV, while a 0.60 eV negative shift relative to pure MoS_2 further confirmed interfacial charge redistribution. Similarly, the S 2p peaks (Figure 4d) at 162.06 eV (S $2p_{3/2}$) and 163.16 eV (S $2p_{1/2}$) show a 0.15 eV shift, corroborating strong electronic interactions. Deconvolution of O 1s spectra (Figure 4e) identifies three components: lattice oxygen (O_{lat}, 529.5 ± 0.6 eV), oxygen vacancies (O_{def}, 531.6 ± 0.4 eV), and adsorbed oxygen species (O_{ads}, 532.5 ± 0.6 eV). TiO_2@MoS_2-8 demonstrates elevated O_{def} (22.72%) and O_{ads} (4.58%) concentrations compared to TiO_2, which aligns with its enhanced ESR signal intensity (Figure 4f) reflecting higher oxygen vacancy density. These synergistic effects of enhanced charge transfer and oxygen-mediated surface activity collectively improved toluene-sensing performance by promoting gas adsorption and redox reactions at the heterojunction interface.

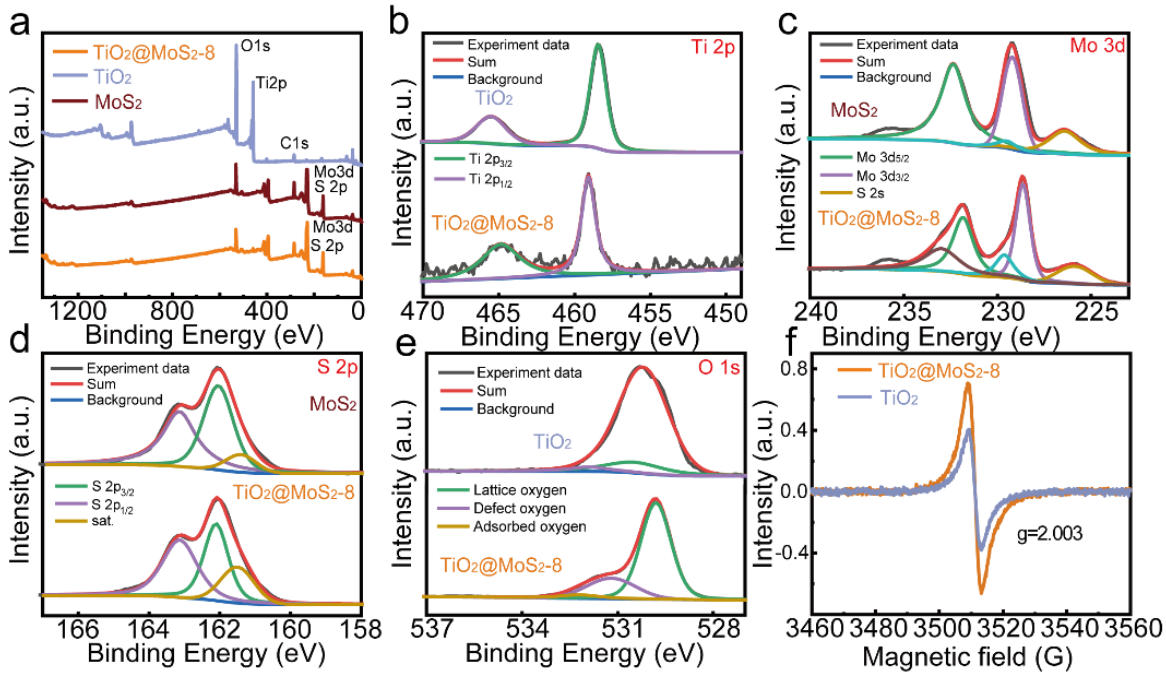


Figure 4. (**a**) X-ray photoelectron spectroscopy (XPS) survey spectra of TiO_2, MoS_2, and TiO_2@MoS_2-8; (**b**) high-resolution Ti 2p spectra of TiO_2 and TiO_2@MoS_2-8; (**c**) Mo 3d spectra of MoS_2 and TiO_2@MoS_2-8; (**d**) S 2p spectra of MoS_2 and TiO_2@MoS_2-8; (**e**) O 1s spectra of MoS_2 and TiO_2@MoS_2-8; (**f**) electron spin resonance (ESR) spectra of TiO_2 and TiO_2@MoS_2-8.

3.2. Gas-Sensitive Property

TiO_2@MoS_2 nanocomposites show great potential as chemiresistive gas sensors due to their high surface area and hierarchical 2D structures. The operating temperature affects surface resistance by altering adsorbed oxygen species and reaction kinetics. This is due to faster surface reactions at higher temperatures competing with reduced gas molecule adsorption because of fewer available active sites [26]. Temperature-dependent sensing tests were conducted from 200 to 280 °C for MoS_2, TiO_2@MoS_2-4, TiO_2@MoS_2-8, and TiO_2@MoS_2-12. The temperature-dependent response exhibited a characteristic volcano profile (Figure 5a), peaking at 240 °C. Below this temperature, inadequate thermal activation hindered oxygen ionosorption and toluene oxidation. Beyond 240 °C, accelerated desorption prevailed over surface reactions, reducing sensor response value [27]. The TiO_2@MoS_2-8 composite achieved a maximum response of 9.8@10 ppm toluene, representing a 3.5-fold enhancement over pristine MoS_2 (2.8), primarily due to oxygen vacancy-mediated toluene adsorption. Notably, TiO_2@MoS_2-8 exhibited rapid response/recovery kinetics (9 s/16 s, Figure 5b), outperforming other samples (MoS_2: 4.1 s/18 s; TiO_2@MoS_2-4: 10 s/17 s; TiO_2@MoS_2-12: 12 s/20 s), benefiting from its optimized mesoporous structure facilitating gas diffusion. Selectivity tests against xylene, benzene, triethylamine, acetone, methanol, ethanol, and ammonia (Figure 5c) revealed superior toluene selectivity. Even under simulated exhaled breath conditions containing mixed interferents (Figure 5d), the sensor maintained stable toluene detection, confirming its robustness in complex environments. These critical attributes of high sensitivity, rapid reaction kinetics, and selective discrimination collectively establish TiO_2@MoS_2 nanocomposites as promising materials for toluene detection applications.

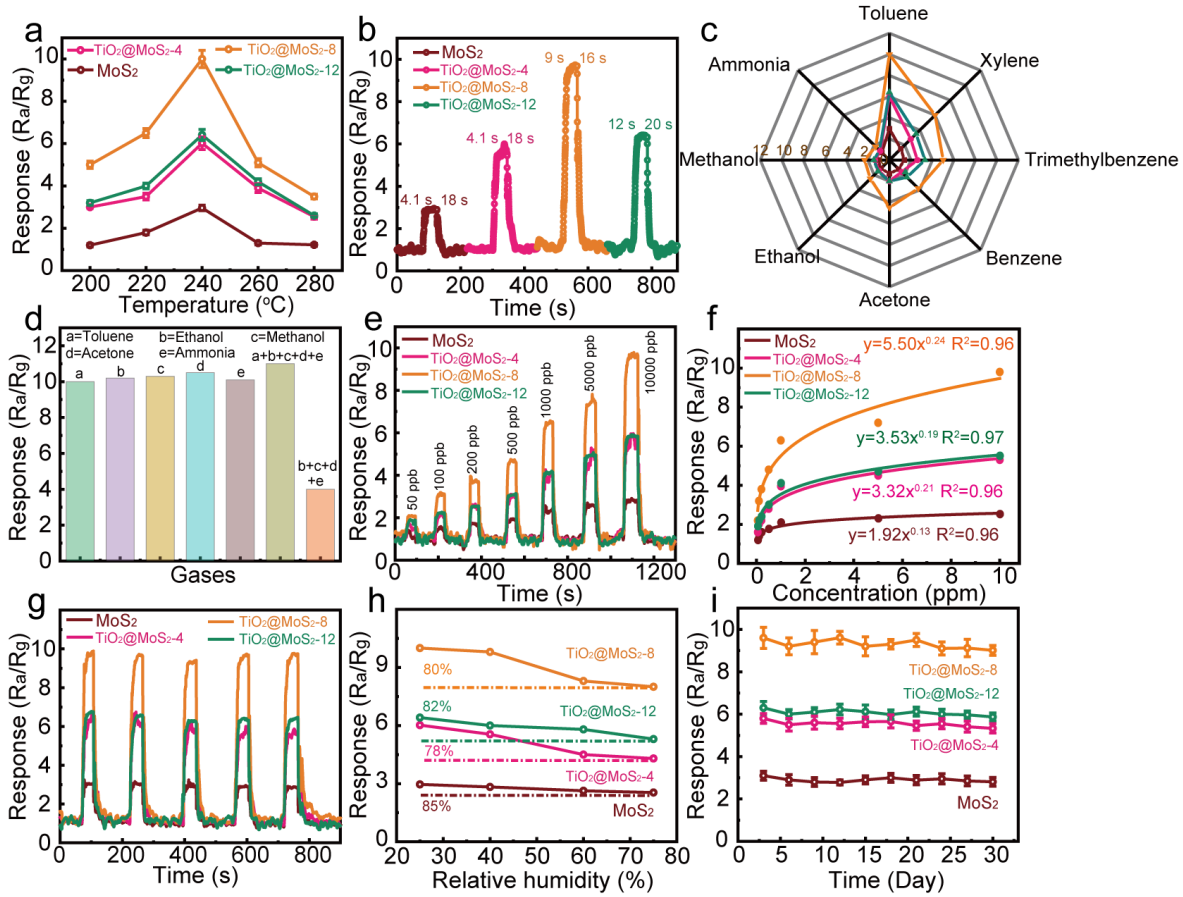


Figure 5. (**a**) Response (R_a/R_g) of MoS_2, TiO_2@MoS_2-4, TiO_2@MoS_2-8, and TiO_2@MoS_2-12 to 10 ppm toluene across 200–280 °C; (**b**) response/recovery time; (**c**) selectivity toward 10 ppm toluene, xylene, benzene, triethylamine, acetone, methanol, ethanol, and ammonia; (**d**) gas responses to mixed vapors at 240 °C; (**e**) dynamic response curves for varied toluene concentrations (0.05–10 ppm) at 240 °C; (**f**) relationship between sensor response and toluene concentrations (0.05–10 ppm); (**g**) reproducibility over five cycles at 10 ppm toluene (240 °C); (**h**) humidity-dependent responses (25 °C, 25–75% RH); (**i**) long-term stability (30 days, 10 ppm).

Figure 5e illustrates the dynamic response of TiO_2@MoS_2-based sensors to varying concentrations of toluene gas, ranging from 50 ppb to 10 ppm. The sensor response demonstrates stepwise enhancement with increasing concentration, with TiO_2@MoS_2 composites exhibiting superior sensitivity compared to pristine MoS_2, particularly at higher concentrations. A limit of detection (LOD) of 50 ppb was achieved for the optimal TiO_2@MoS_2-8 sensor. As shown in Figure 5f, all samples maintain linear responses across the 0.05–10 ppm range, validating quantitative detection capability. Repeatability tests (Figure 5g) revealed stable performance over five cycles at 10 ppm, with response variations below ±5.2%. Under humidity challenges (25%–75% RH, Figure 5h), the response attenuation remained <20%, underscoring robust moisture resistance. Long-term stability assessments (30 days exposure to 10 ppm toluene, Figure 5i) showed <8% signal drift, confirming durability for practical deployment. Table 1 shows the comparison of sensor-based toluene gas detection characteristics with different detection materials, further confirming the great potential of TiO_2@MoS_2-based material as a toluene sensor due to its lower detection limit and rapid response/recovery time.

Table 1. Comparison of sensor-based toluene gas detection characteristics with different detection materials.

Materials	T (°C)	Concentration (ppm)	Detection Limit (ppm)	T_{res}/T_{rec} (s)	Ref.
Pd/PdO-decorated SnO_2	285	100	0.05	50/138	[28]
V_2C MXene	25	200	0.047	14/34	[29]
SnO_2-decorated NiO	100	250	0.01	-	[30]
MoS_2-Fe_3O_4	25	20	5	58/23	[7]
ZnO@Co_3O_4	290	100	5	11.2/12.5	[16]
NiO/ZnO	100	300	0.1	2/33	[17]
TiO_2@MoS_2	240	10	0.05	9/16	This work

As shown in Figure 6a, time-resolved in situ Fourier transform infrared (in situ FTIR) spectroscopy was employed to analyze intermediate products during toluene sensing. Peaks observed in the 1450–1600 cm^{-1} range originate from C=C aromatic ring vibrations, with increasing intensity over time indicating progressive aromatic compound accumulation. Absorption bands between 1370–1450 cm^{-1} correspond to C-H bending modes of methyl groups directly bonded to the benzene ring, confirming toluene decomposition. Concurrently, diminishing toluene-specific peaks and emerging signals at 3000–3100 cm^{-1} (aromatic C-H stretching) suggest catalytic conversion pathways where toluene transforms into benzene derivatives. Resistance changes in TiO_2@MoS_2 nanocomposites arise from oxygen-mediated surface interactions: at 240 °C, chemisorbed oxygen species (O_2^-, O^-) populate oxygen vacancies, forming electron-depletion layers that reduce baseline resistance in air (Equation (4)) [31]. Upon toluene exposure, adsorbed oxygen species react with methyl groups via stepwise dehydrogenation (Equations (5)–(8)), modulating conductivity through electron transfer between the semiconductor and reaction intermediates. This mechanistic framework aligns with the observed spectral evolution and sensor response dynamics.

$$O_2(g) \rightarrow O_2(ads) \quad (4)$$

$$O_2(ads) + e^- \rightarrow O_2^-(ads) \quad (5)$$

$$O_2^-(ads) + e^- \rightarrow 2O^-(ads) \quad (6)$$

$$C_7H_8(g) + 3O^-(ads) \rightarrow C_6H_6(g) + CO_2 + H_2O(g) + 3e^- \quad (7)$$

$$C_6H_6(g) + 15O^-(ads) \rightarrow 6CO_2 + 3H_2O(g) + 15e^- \quad (8)$$

The enhanced toluene-sensing performance of the 2D stacked MoS_2@TiO_2 heterostructure compared to pristine MoS_2 and TiO_2 nanosheets arises from three synergistic mechanisms, as follows.

(I) Hierarchical architecture and surface engineering. Gas–solid interactions in chemiresistive sensors critically depend on surface-mediated oxygen adsorption and target gas diffusion. The MoS_2@TiO_2 heterostructure exhibits a superior specific surface area, providing abundant active sites for oxygen chemisorption. The vertically aligned MoS_2 nanosheets on TiO_2 substrates prevent nanosheet restacking while creating interconnected nanochannels that enhance toluene diffusion kinetics.

(II) Interface charge redistribution in n–n heterojunctions. The work function disparity between MoS_2 (Φ = 4.05 eV) and TiO_2 (Φ = 4.77 eV), determined by ultraviolet photoelectron spectroscopy (UPS, Figure S3), drives interfacial electron transfer from TiO_2 to MoS_2 [32,33]. This creates a built-in electric field at the heterointerface, forming an electron-depletion layer, which lowers the oxygen adsorption activation energy and facilitates hole–electron

separation efficiency [34]. Band alignment analysis (Figure S2) reveals heterojunction characteristics with MoS_2 and TiO_2 bandgaps of 3.20 eV and 0.85 eV, respectively [35–37]. The conduction band offset promotes electron trapping by adsorbed oxygen species (O_2^-/O^-), amplifying resistance modulation upon toluene exposure.

(III) Influence by oxygen species. Compared with TiO_2 nanosheets, TiO_2@MoS_2 has the highest ESR intensity and the highest relative concentration of oxygen vacancy. Therefore, the TiO_2@MoS_2 hierarchical structure can provide additional O_{ads} and O_{def}, which is conducive to the reaction of the target gas with oxygen, while increasing the surface active site, which is conducive to the sensing performance of toluene [38,39].

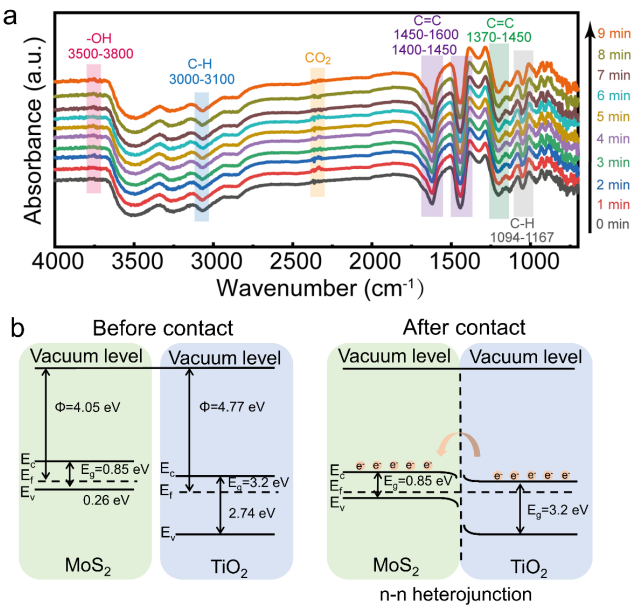


Figure 6. (**a**) In situ DRIFTS analysis of the TiO_2@MoS_2-8 nanocomposite during gas exposure; (**b**) band alignment diagrams illustrating the interfacial energy structure of TiO_2 and MoS_2 pre- and post-heterojunction formation.

4. Conclusions

In summary, TiO_2@MoS_2 core–shell heterostructures were fabricated by assembling MoS_2 nanosheet arrays onto TiO_2 nanosheets prepared via a sacrificial template method. The unique 2D hierarchical heterojunction structure resulted in a larger specific surface area and increased generation of oxygen vacancies. Compared with individual TiO_2 nanosheets and MoS_2 nanosheets, the TiO_2@MoS_2 composite demonstrated the highest response (R_a/R_g = 9.8@10 ppm toluene) at 240 °C. Furthermore, the hierarchical TiO_2@MoS_2 core–shell structure exhibited fast response/recovery times (9 s/16 s), a low detection limit (50 ppb), excellent selectivity, and robust stability in humid environments. The enhanced gas-sensing performance is attributed to the synergistic effects between the two components and the distinctive core–shell hierarchical architecture with self-assembled nanostructures. This work provides a rational material structure design strategy, offering a promising candidate for detecting toluene gas, thereby demonstrating significant potential value for advancing environmental or disease diagnosis detection.

Supplementary Materials: The following supporting information can be downloaded at https://www.mdpi.com/article/10.3390/chemosensors13050154/s1. Figure S1: Ceramic plate and test base; Figure S2: (a–d) UV-vis diffuse reflectance spectra (DRS) of TiO_2 and MoS_2 nanosheets with corresponding Tauc plots for bandgap determination; Figure S3: Ultraviolet photoelectron spectroscopy

(UPS) spectra of pristine TiO_2 and MoS_2 recorded under He I_α excitation (21.22 eV), showing secondary electron cutoff (left) and valence band regions (right).

Author Contributions: D.W. (Dehui Wang): Investigation; writing original draft; conceptualization; visualization. J.H.: Investigation; conceptualization; writing original draft. H.X.: Writing, review & editing; project administration. D.W. (Ding Wang): Funding acquisition; project administration; writing, review & editing. G.L.: Funding acquisition; project administration. All authors have read and agreed to the published version of the manuscript.

Funding: The authors greatly appreciate the financial support from National Natural Science Foundation of China (62471303, 62071300, 22176127, 22301181, 22406130, 22476131), Shanghai Sailing Program (23YF1429000, 22YF1430400). We also acknowledge the USST Center for Instrumental Analysis for their support in materials characterization and High Performance Computing Center of USST for their support in the calculations.

Institutional Review Board Statement: Not applicable.

Informed Consent Statement: Not applicable.

Data Availability Statement: The raw data supporting the conclusions of this article will be made available by the authors on request.

Acknowledgments: We acknowledge the USST Center for Instrumental Analysis for their support in material characterization.

Conflicts of Interest: The authors declare no conflict of interest.

References

1. Ueda, T.; Hayashi, H.; Tsukahara, R.; Shimizu, Y.; Hyodo, T. Effects of Structure and Thickness of $Ce_{0.9}Pr_{0.1}O_2$ Electrodes of YSZ-Based Gas Sensors on VOC-Sensing Properties. *Sens. Actuators B Chem.* **2025**, *422*, 136580. [CrossRef]
2. Zhang, Y.-L.; Jia, C.-W.; Tian, R.-N.; Guan, H.-T.; Chen, G.; Dong, C.-J. Hierarchical Flower-like $NiFe_2O_4$ with Core–Shell Structure for Excellent Toluene Detection. *Rare Met.* **2021**, *40*, 1578–1587. [CrossRef]
3. Wang, T.; Liu, S.; Sun, P.; Wang, Y.; Shimanoe, K.; Lu, G. Unexpected and Enhanced Electrostatic Adsorption Capacity of Oxygen Vacancy-Rich Cobalt-Doped In_2O_3 for High-Sensitive MEMS Toluene Sensor. *Sens. Actuators B Chem.* **2021**, *342*, 129949. [CrossRef]
4. Liao, Z.; Chu, N.; Yuan, Z.; Shen, Y.; Meng, F. Highly Sensitive Toluene Sensor Based on Silver Ear-Like F-Doped Co_3O_4 Templated from Co(OH)F Guided by SiO_2 Nanospheres. *Chem. Eng. J.* **2024**, *498*, 155688. [CrossRef]
5. Zhang, H.; Hu, J.; Li, M.; Li, Z.; Yuan, Y.; Yang, X.; Guo, L. Highly Efficient Toluene Gas Sensor Based on Spinel Structured Hollow Urchin-like Core-Shell $ZnFe_2O_4$ Spheres. *Sens. Actuators B Chem.* **2021**, *349*, 130734. [CrossRef]
6. Siraj, S.; Bansal, G.; Hasita, B.; Srungaram, S.; S, S.K.; Rybicki, F.J.; Sonkusale, S.; Sahatiya, P. MXene/MoS_2 Piezotronic Acetone Gas Sensor for Management of Diabetes. *ACS Appl. Nano Mater.* **2024**, *7*, 11350–11361. [CrossRef]
7. Thayil, R.; Krishna, K.G.; Cherukulappurath, S.; Kathirvelu, V.; Parne, S.R. MoS_2 and MoS_2-Based Nanocomposites for Enhanced Toluene Sensing Response at Room Temperature. *Surf. Interfaces* **2024**, *46*, 104134. [CrossRef]
8. Tang, T.; Li, Z.; Liu, Y.Y.; Chen, Y.L.; Cheng, Y.F.; Liang, Y.; Zhuang, J.H.; Hu, X.Y.; Jannat, A.; Ou, R.; et al. Ultrathin two-dimensional titanium oxysulfide for enhanced sensitivity and stability of room temperature NO_2 sensing. *Ceram. Int.* **2025**, *51*, 3216–3223. [CrossRef]
9. Guan, X.; Zhao, L.; Zhang, P.; Liu, J.; Song, X.; Gao, L. Electrode Material of Core-Shell Hybrid MoS_2@C/CNTs with Carbon Intercalated Few-Layer MoS_2 Nanosheets. *Mater. Today Energy* **2020**, *16*, 100379. [CrossRef]
10. Gough, J.J.; McEvoy, N.; O' Brien, M.; Bell, A.P.; McCloskey, D.; Boland, J.B.; Coleman, J.N.; Duesberg, G.S.; Bradley, A.L. Dependence of Photocurrent Enhancements in Quantum Dot (QD)-Sensitized MoS_2 Devices on MoS_2 Film Properties. *Adv. Funct. Mater.* **2018**, *28*, 1706149. [CrossRef]
11. Zhang, W.; Liu, Y.; Pei, X.; Yuan, Z.; Zhang, Y.; Zhao, Z.; Hao, H.; Long, R.; Liu, N. Stretchable MoS_2 Artificial Photoreceptors for E-Skin. *Adv. Funct. Mater.* **2022**, *32*, 2107524. [CrossRef]
12. Chen, Y.L.; Li, Z.; Tang, T.; Cheng, Y.F.; Cheng, L.; Wang, X.X.; Haidry, A.A.; Jannat, A.; Ou, J.Z. Room-Temperature Optoelectronic NO_2 Sensing Using Two-Dimensional Gallium Oxyselenides. *ACS Appl. Nano Mater.* **2024**, *7*, 3229–3238. [CrossRef]
13. Wang, H.; Shao, Z.; Shi, X.; Tang, Z.; Sun, B. Rapidly Detecting the Carcinogen Acetaldehyde: Preparation and Application of a Flower-like MoS_2 Cataluminescence Sensor at Low Working Temperature. *Anal. Methods* **2023**, *15*, 5620–5629. [CrossRef] [PubMed]

14. Niu, Y.; Zeng, J.; Liu, X.; Li, J.; Wang, Q.; Li, H.; de Rooij, N.F.; Wang, Y.; Zhou, G. A Photovoltaic Self-Powered Gas Sensor Based on All-Dry Transferred MoS_2/GaSe Heterojunction for ppb-Level NO_2 Sensing at Room Temperature. *Adv. Sci.* **2021**, *8*, 2100472. [CrossRef] [PubMed]
15. Cheng, X.; Yao, Y.T.; Zheng, S.L.; Wan, Y.; Wei, C.D.; Yang, G.C.; Yuan, Y.; Tsai, H.-S.; Wang, Y.; Hao, J.Y. Te@Se Core–Shell Heterostructures with Tunable Shell Thickness for Ultra-Stable NO_2 Detection. *ACS Sens.* **2025**, *10*, 283–291. [CrossRef]
16. Shi, J.; Xiong, J.; Qiao, L.; Liu, C.; Zeng, Y. Facile MOF-on-MOF Isomeric Strategy for ZnO@Co_3O_4 Single-Shelled Hollow Cubes with High Toluene Detection Capability. *Appl. Surf. Sci.* **2023**, *609*, 155271. [CrossRef]
17. Liu, H.; Wang, Z.; Cao, G.; Pan, G.; Yang, X.; Qiu, M.; Sun, C.; Shao, J.; Li, Z.; Zhang, H. Construction of Hollow NiO/ZnO p-n Heterostructure for Ultrahigh Performance Toluene Gas Sensor. *Mater. Sci. Semicond. Process.* **2022**, *141*, 106435. [CrossRef]
18. Ma, S.; Xu, J. Nanostructured Metal Oxide Heterojunctions for Chemiresistive Gas Sensors. *J. Mater. Chem. A* **2023**, *11*, 23742–23771. [CrossRef]
19. Wang, Y.; Tan, L.; Tan, M.H.; Zhang, P.P.; Yoshiharu, Y.; Yang, G.H.; Tsubaki, N. Rationally Designing Bifunctional Catalysts as an Efficient Strategy to Boost CO_2 Hydrogenation Producing Value-Added Aromatics. *ACS Catal.* **2018**, *9*, 895–901. [CrossRef]
20. Hermawan, A.; Asakura, Y.; Inada, M.; Yin, S. A Facile Method for Preparation of Uniformly Decorated-Spherical SnO_2 by CuO Nanoparticles for Highly Responsive Toluene Detection at High Temperature. *J. Mater. Sci. Technol.* **2020**, *51*, 119–129. [CrossRef]
21. Liu, H.; Wang, Z.; Sun, C.; Shao, J.; Li, Z.; Zhang, H.; Qiu, M.; Pan, G.; Yang, X. Construction of Co_3O_4/Fe_3O_4 Heterojunctions from Metal Organic Framework Derivatives for High Performance Toluene Sensor. *Sens. Actuators B Chem.* **2023**, *375*, 132863. [CrossRef]
22. Raghu, A.V.; Karuppanan, K.K.; Nampoothiri, J.; Pullithadathil, B. Wearable, Flexible Ethanol Gas Sensor Based on TiO_2 Nanoparticles-Grafted 2D-Titanium Carbide Nanosheets. *ACS Appl. Nano Mater.* **2019**, *2*, 1152–1163. [CrossRef]
23. Cao, S.; Sui, N.; Zhang, P.; Zhou, T.; Tu, J.; Zhang, T. TiO_2 Nanostructures with Different Crystal Phases for Sensitive Acetone Gas Sensors. *J. Colloid Interf. Sci.* **2022**, *607*, 357–366. [CrossRef]
24. Zhao, Y.; Song, J.-G.; Ryu, G.H.; Ko, K.Y.; Woo, W.J.; Kim, Y.; Kim, D.; Lim, J.H.; Lee, S.; Lee, Z.; et al. Low-Temperature Synthesis of 2D MoS_2 on a Plastic Substrate for a Flexible Gas Sensor. *Nanoscale* **2018**, *10*, 9338–9345. [CrossRef]
25. Kumar, R.; Zheng, W.; Liu, X.; Zhang, J.; Kumar, M. MoS_2-Based Nanomaterials for Room-Temperature Gas Sensors. *Adv. Mater. Technol.* **2020**, *5*, 1901062. [CrossRef]
26. Verma, G.; Gokarna, A.; Kadiri, H.; Nomenyo, K.; Lerondel, G.; Gupta, A. Multiplexed Gas Sensor: Fabrication Strategies, Recent Progress, and Challenges. *ACS Sens.* **2023**, *8*, 3320–3337. [CrossRef]
27. Korotcenkov, G.; Cho, B.K. Metal Oxide Composites in Conductometric Gas Sensors: Achievements and Challenges. *Sens. Actuators B Chem.* **2017**, *244*, 182–210. [CrossRef]
28. Gong, C.; Chen, M.; Song, F.; Yin, P.; Zhao, X.; You, X.; Fu, H.; Yu, S.; Liu, X.; Zhang, K.; et al. A Highly Sensitive Toluene Gas Sensor Based on Pd/PdO Decorated SnO_2 Prepared by Electrospinning. *ACS Appl. Electron. Mater.* **2024**, *6*, 6036–6048. [CrossRef]
29. Karmakar, S.; Deepak, M.S.; Nanda, O.P.; Sett, A.; Maity, P.C.; Karmakar, G.; Sha, R.; Badhulika, S.; Bhattacharyya, T.K. 2D V_2 C MXene Based Flexible Gas Sensor for Highly Selective and Sensitive Toluene Detection at Room Temperature. *ACS Appl. Electron. Mater.* **2024**, *6*, 3717–3725. [CrossRef]
30. Gao, H.; Zhao, L.; Wang, L.; Sun, P.; Lu, H.; Liu, F.; Chuai, X.; Lu, G. Ultrasensitive and Low Detection Limit of Toluene Gas Sensor Based on SnO_2-Decorated NiO Nanostructure. *Sens. Actuators B Chem.* **2018**, *255*, 3505–3515. [CrossRef]
31. Jung, G.; Shin, W.; Hong, S.; Jeong, Y.; Park, J.; Kim, D.; Bae, J.-H.; Park, B.-G.; Lee, J.-H. Comparison of the Characteristics of Semiconductor Gas Sensors with Different Transducers Fabricated on the Same Substrate. *Sens. Actuators B Chem.* **2021**, *335*, 129661. [CrossRef]
32. Hu, J.W.; Wang, F.; Yu, J.J.; Hong, Z.J.; Zhang, W.H.; Li, H.-J.; Lai, Z.C.; Wang, D.; Deng, Y.H.; Li, G.S. MOF-derived porous Co_3O_4 nanosheets array assembled on SnO_2 nanofibers for humidity-resistant high efficiency acetone detection. *Chin. Chem. Lett.* **2025**, 110863. [CrossRef]
33. Lashkov, A.V.; Fedorov, F.S.; Vasilkov, M.Y.; Kochetkov, A.V.; Belyaev, I.V.; Plugin, I.A.; Varezhnikov, A.S.; Filipenko, A.N.; Romanov, S.A.; Nasibulin, A.G.; et al. The Ti Wire Functionalized with Inherent TiO_2 Nanotubes by Anodization as One-Electrode Gas Sensor: A Proof-of-Concept Study. *Sens. Actuators B Chem.* **2020**, *306*, 127615. [CrossRef]
34. Shokri, A.; Salami, N. Gas Sensor Based on MoS_2 Monolayer. *Sens. Actuators B Chem.* **2016**, *236*, 378–385. [CrossRef]
35. Hou, J.-L.; Lin, Y.-T.; Hsueh, T.-J. Room-Temperature TiO_2 Gas Sensor with Conical-TSV Using a Thermal Oxidation Process. *ACS Appl. Electron. Mater.* **2023**, *5*, 6542–6548. [CrossRef]
36. Liu, H.; Shen, W.; Chen, X. A Room Temperature Operated Ammonia Gas Sensor Based on Ag-Decorated TiO_2 Quantum Dot Clusters. *RSC Adv.* **2019**, *9*, 24519–24526. [CrossRef]
37. Hu, J.W.; Zou, Y.D.; Deng, Y.; Li, H.-J.; Xu, H.; Wang, D.; Wu, L.M.; Deng, Y.H.; Li, G.S. Recent Advances in Non-Ionic Surfactant Templated Synthesis of Porous Metal Oxide Semiconductors for Gas Sensing Applications. *Prog. Mater. Sci.* **2025**, *150*, 101409. [CrossRef]

38. Hou, L.; Duan, J.; Xiong, F.; Carraro, C.; Shi, T.; Maboudian, R.; Long, H. Low Power Gas Sensors: From Structure to Application. *ACS Sens.* **2024**, *9*, 6327–6357. [CrossRef]
39. Doan, T.H.P.; Ta, Q.T.H.; Sreedhar, A.; Hang, N.T.; Yang, W.; Noh, J.-S. Highly Deformable Fabric Gas Sensors Integrating Multidimensional Functional Nanostructures. *ACS Sens.* **2020**, *5*, 2255–2262. [CrossRef]

Disclaimer/Publisher's Note: The statements, opinions and data contained in all publications are solely those of the individual author(s) and contributor(s) and not of MDPI and/or the editor(s). MDPI and/or the editor(s) disclaim responsibility for any injury to people or property resulting from any ideas, methods, instructions or products referred to in the content.